Ultrafast laser-induced extrusion of mono-crystalline nano-pillars from sapphire

VALERIA V. BELLONI,[1] ANNE-MAGALI SEYDOUX-GUILLAUME,[2] SERGIO SAO-JOAO,[3] MOSTAFA HASSAN,[1] LUCA FURFARO,[1] REMO GIUST,[1] AND FRANCOIS COURVOISIER [1,*]

[1] *Université Marie et Louis Pasteur, CNRS, institut FEMTO-ST, F-25000 Besançon, France*
[2] *CNRS, Université Jean Monnet Saint-Étienne, Laboratoire de Géologie de Lyon: Terre, Planètes, Environnement (LGL-TPE), UMR5276, F-42023, SAINT-ETIENNE, FRANCE*
[3] *Mines Saint-Etienne, CNRS, UMR 5307 LGF, Centre SMS, Saint-Etienne, F-42023 France*
[*] *francois.courvoisier@femto-st.fr*

Abstract:

A single ultrafast laser pulse, shaped as a radially polarized first-order Bessel beam, induces the formation of high aspect ratio nano-pillars emerging from the bulk of sapphire in a laser-induced extrusion process. Three distinct regimes could be observed depending on laser fluence, ranging from straight nano-pillars to nano-structures shaped by capillary instability. Here, we report Transmission Electron Microscopy (TEM) and Transmission Kikuchi Diffraction (TKD) structural analysis to reveal the underlying formation mechanisms of the nano-structures for all the three regimes. We demonstrate, using crystalline orientation analysis, that they range from the translation of a crystalline rod to the resolidification of a hydrodynamic jet of molten sapphire. Remarkably, all nano-pillars are monocrystalline sapphire. The TEM structural analysis of the materials below the surface also provides new insights into the complex phenomena following the laser-matter interaction and the processes underlying the formation of these structures.

1. Introduction

Ultrafast laser pulses can induce phase changes in various materials, including semiconductors [1–3], dielectrics [4, 5], and metals [6, 7]. In dielectrics, the nonlinear ionization process allows for material modifications within the volume without affecting the surfaces [8, 9]. This is not only ideal for three-dimensional structuring [10] but also generates extreme thermodynamic conditions relevant to the interior of stellar objects such as planetary interiors or brown dwarfs, which is Warm Dense Matter [11]. When ultrafast laser pulses are tightly focused inside materials like glass or sapphire, they cause optical breakdown and subsequent micro-explosions within the bulk material [12–16]. In sapphire, a single laser pulse causes the formation of a dense amorphous phase in which nano-crystallites of dense bcc-Al were for the first time found [17].

Bessel beams are a promising route to extend the process to much larger volumes in dielectrics. A zeroth-Bessel beam forms an elongated focus, *i.e.*, a line-focus, formed by the interference of an infinite set of plane waves directed with the same angle θ toward the optical axis in cylindrical symmetry [18]. Single shot ultrafast laser pulses shaped as zeroth-order Bessel beams can generate extremely high aspect ratio nano-voids, with a length that can largely exceed several tens of micrometers and extend up to centimeter-scale [19–21]. The dynamics of these voids have been characterized at nanosecond timescales in quartz using optical methods [22]. A zeroth-order Bessel beam creates a shock oriented outwards that quickly dissipates with radial distance from the line focus. In contrast, a first-order Bessel beam has a cylindrical focus, capable of producing both inward and outward-propagating shockwaves. In the ultrafast regime, this generates a cylindrical plasma that can compress the material inside [23].

We have recently reported the formation of nano-pillars on the surface of sapphire by exciting the material beneath the surface with a single pulse shaped as a radially-polarized first-order Bessel beam [24]. These nano-pillars have a high aspect ratio, with a typical diameter of 800 nm,

corresponding to the diameter of the cylindrical focus of the Bessel beam, and heights up to 15 µm. The morphologies of the nano-pillars suggest three formation regimes controlled by the laser fluence on the sample exit side. To better understand the formation processes, it is crucial to investigate the structural information about the pillars themselves and the material below, which sustained a cylindrical micro-explosion. Transmission Electron Microscopy and Transmission Kikutchi Diffraction allow the analysis of crystallinity, defect arrangements and the presence of any amorphous phase. Our findings support the formation mechanisms ranging from the translation of a rod of solid sapphire to a jet of molten sapphire. Remarkably, despite varying formation conditions, all nano-pillars remain monocrystalline, even when resolidified into exotic shapes.

After describing the laser processing and characterization procedures in Section II, we analyze and draw conclusions for each regime: translation of a crystalline rod (Sec. III), extrusion of viscous sapphire (Sec. IV) and hydrodynamic jet of liquid sapphire (Sec. V).

2. Experimental procedure

2.1. Generation of sapphire nano-pillars by single femtosecond laser pulse

To generate nano-pillars on top of sapphire surface with a single laser pulse [24], we used a Ti:Sapphire laser source with a pulse duration of 115 fs (FWHM) and central wavelength 800 nm. A spatial light modulator, a 2f-2f telescopic system, composed of 0.75 m lens and a ×50 microscope objective with 0.8 numerical aperture, and a radial polarization converter allow obtaining a radially polarized Bessel beam with a length of 20 µm (FWHM) and a cone angle $\theta = 36°$ (more detail on the setup in ref. [24]). The beam characterization is performed using a second 2f-2f telescope including an identical microscope objective, associated to a CMOS camera. The superposition of a radial polarization on a zeroth-order Bessel beam gives a transverse intensity distribution describable by a first-order Bessel function. Thus, the beam is composed of an elongated hollow cylinder, *i.e.* the cylindrical focus, with a diameter of 800 nm surrounded by concentric lobes of weaker intensity. A cross-cut of the beam is shown in Fig. 1a. The peak intensity exceeds 10^{14} W.cm^2. During pulse propagation, nonlinear ionization generates a dense plasma of free-electrons [25]. Despite the high intensity, the impact of Kerr effect on the beam shape is negligible because of the very strong focusing. Strongly focused higher-order Bessel beams are known to preserve their shape even at high-intensity [23].

We worked on a c-cut sapphire sample (thickness 150 µm) with the beam straddling the rear surface of the sample. A sketch of the laser processing configuration is shown in Fig. 1b with the curve of the central core fluence along the propagation direction as a black line.

Figure 1c reports the SEM (Scanning Electron Microscopy) images of three nano-pillars representative of the three main morphologies. They were all obtained with a pulse energy of 6.1 µJ and different relative beam-to-surface positions. The relative exit surface fluence, which is one of the essential parameters to control the morphology of the nano-pillar, is estimated to 1, 3, and 6. At low fluence, the nano-pillars have vertical and straight walls (Fig. 1d). In this first regime, the nano-pillars are around 4 µm in height and 800 nm in diameter. Increasing the fluence, we observe a second regime in which the nano-pillars are higher and present a deformed tip (Fig. 1e). In this regime, the nano-pillars can exceed 10 µm with a variable diameter along the nano-pillar. For even higher fluences, we observe a third regime in which the nano-pillars are very wavy (Fig. 1f). The nano-pillars of the third regime show a remarkable range in height, from 5 µm to more than 15 µm.

The mechanism we hypothesized to explain the different morphologies is the following. During the ultrafast laser pulse propagation inside sapphire, nonlinear ionization generates a hollow cylindrical nano-plasma, with a local temperature and pressure distribution fixed by the laser pulse fluence. The fluence distribution on the Bessel beam cylindrical focus varies with propagation: it is higher inside the sample than closer to the surface. In the first regime, for the lowest fluence,

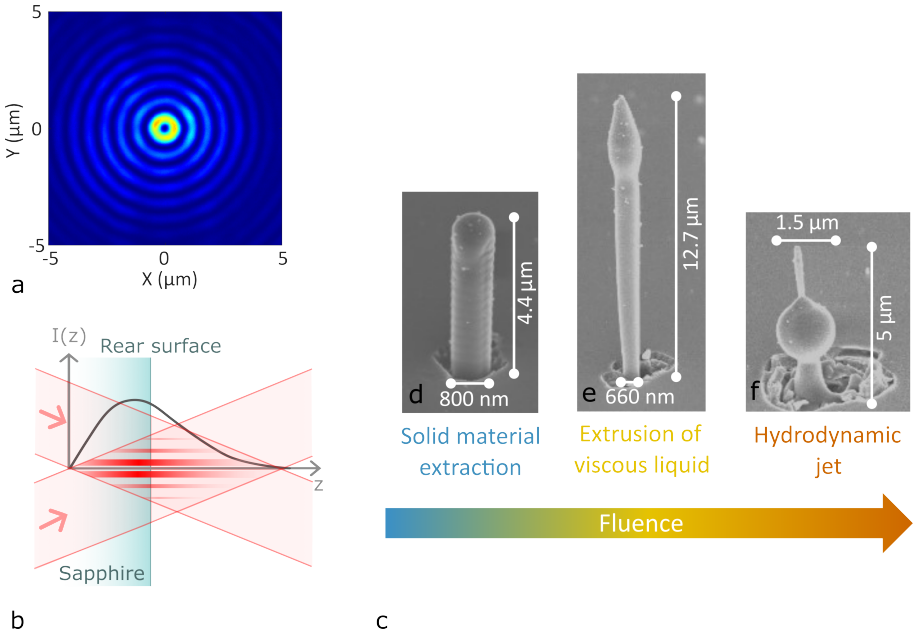

Fig. 1. (a) Cross-cut of the experimental intensity distribution of beam shaped as first order Bessel beam. (b) Scheme of the processing with the beam crossing the rear surface of the sample. The black line shows the evolution of the intensity along the propagation direction. (c) Different nano-pillar morphologies obtained by increasing the fluence of the main beam lobe on the rear surface of the sample.

the energy deposited close to the sample exit surface is enough to create a thin cylindrical layer of liquid material which allows an internal solid rod to translate across the surface due to pressure gradients. In the second regime, we hypothesized that the higher fluence allows the internal rod of material to partially melt and be ejected. In the last regime, the most intense part of the beam is close to the exit surface. We suppose that the nano-pillars are created by a jet of liquid material undergoing capillary instabilities.

2.2. Transmission Electron Microscopy investigations

We performed Transmission Electron Microscopy (TEM) measurements to obtain structural information of the laser-modified material and to better understand the generation processes. We have used a Focused Ion Beam (FIB, Thermo Fisher Scientific FEI 125 Helios Nanolab 600i FIB) to obtain TEM foils from the nano-pillars and the bulk material below. To protect the structure, a thick layer of carbon deposition has been deposited on both sides at different angles and at the top of the structure. The TEM foil is then processed to reach a thickness of about 60 nm, and we studied the three nano-pillars shown in Fig. 1 according to this procedure.

In the following figures, we will present different TEM imaging techniques performed with a Cs-corrected TEM (NeoARM200FCold FEG) operated at 200 kV. We will show TEM measurements in Bright Field mode (BF) with different Selected Area Electron Diffraction (SAED). The SAEDs are recorded in the zone axis (*i.e.*, an orientation which represents the direction of a group of crystallographic planes within a crystal) of the bulk and of the nano-pillar to highlight and relate the structure of the two regions. We have also performed Scanning Transmission Electron Microscopy (STEM) measurements in Annular Bright Field (ABF), which highlight inhomogeneities in the crystalline structure, and Annular Dark Field (ADF), which provide

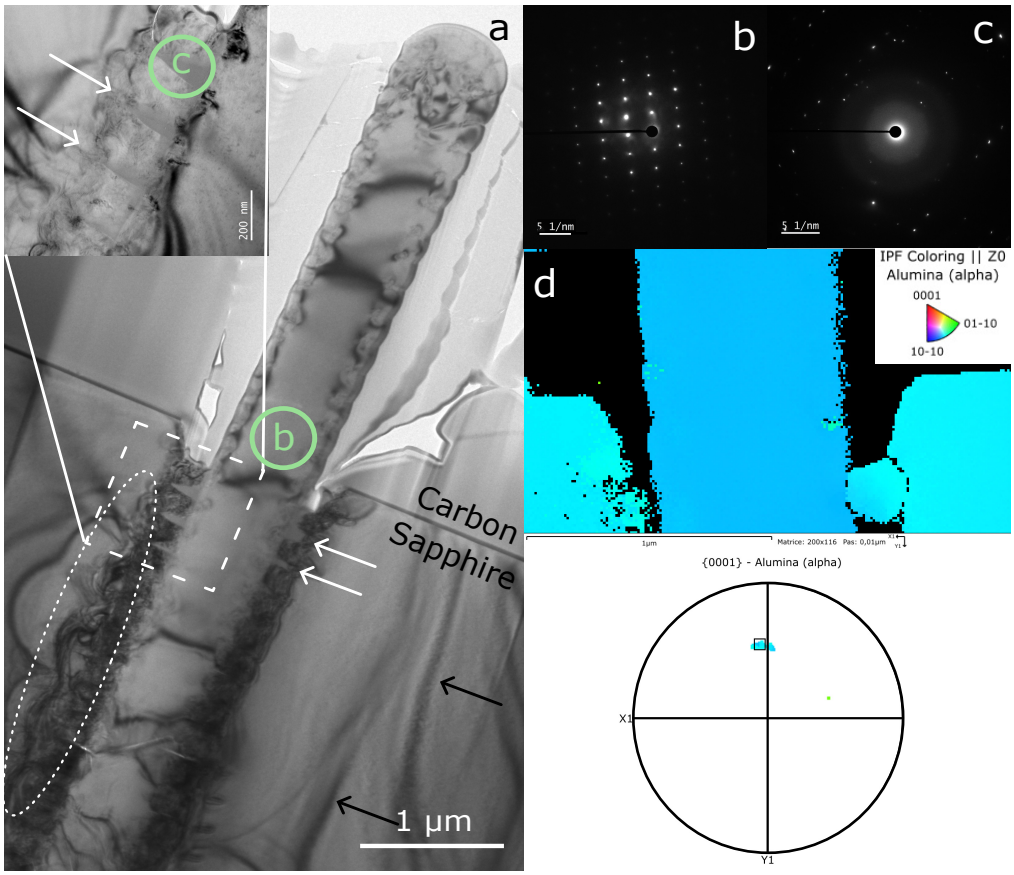

Fig. 2. TEM investigation of the first regime nano-pillar. (a) TEM-BF image of the nano-pillar covered with carbon deposition. (b-c) Selected Area Electron Diffraction of parts of the nano-pillar, indicated with circled letters in (a). (d) IPF figure from TKD measurements of the base of the pillar and part of the bulk with related pole figure.

information on the sample density.

In addition to TEM observations, we performed a Transmission Kikuchi Diffraction (TKD) analysis on the thin foils. TKD provides microstructural information through an excitation volume much smaller than that of the bulk sample in EBSD (Electron BackScatter Diffraction), allowing a spatial resolution on the order of 10 nm to be achieved. Several maps were produced to complement the TEM observations, *e.g.* grain boundaries, IPF Z (Inverse Pole Figure), and KAM (Kernel Average Misorientation). The TKD study was conducted using a Zeiss SUPRA 55VP FEG-SEM system equipped with an Oxford Instruments Symmetry S2 EBSD detector. The maps were acquired using AZTEC HKL software. All measurement parameters are listed in Table S.1 of the Supplemental Material.

3. First regime: translation of a crystalline rod

The pillar of the first regime under investigation is the one shown in Fig. 1d. The nano-pillar is 4.4 µm in height with a diameter of 800 nm. Fig. 2a shows the TEM-BF image of the nano-pillar surrounded by the carbon deposition and part of the bulk.

The pillar exhibits black elongated lines, which are also visible in the bulk (see black arrows in Fig. 2a). These lines are Bragg contrast lines and indicate the crystallinity of the sample.

Therefore, the pillar of the first regime is crystalline, which is further confirmed by the diffraction patterns recorded along its length (an example of SAED is shown in Fig. 2b). The different diffraction patterns are all performed in a similar zone axis [5 1 1], confirming that the nano-pillar is a mono-crystal (SAEDs available in Suppl. Fig. S.1). In addition, we can observe more chaotic Bragg contrast lines at the edges of the nanopillar, suggesting the presence of strong strain.

Further STEM investigations show that the nano-pillar is homogeneous but exhibits some defects, such as dislocations or lattice disorientations (STEM-ADF and STEM-ABF images in Suppl. Fig. S.2). The defects are concentrated in two main regions. The first one is at the tip of the nano-pillar, probably caused by extremely localized melting and relatively rapid resolidification of the tip (which is round while the surface was initially flat). The other defects are equally spaced along the pillar height and correspond to the corrugations on the pillar surface observable in Fig. 1d. In Ref. [24], we identified that this periodic pattern originates from the interference between the incoming Bessel beam and its back-reflection on the rear surface. This induces a periodic intensity pattern with a period of $\frac{\lambda}{2n\cos\theta} = 241$ nm (λ is the central wavelength, n is the sapphire refractive index, and θ the Bessel beam cone angle in the medium). Therefore, the periodic structure must have been produced before the translation of the solid rod.

In the bulk, we observe periodic grey triangular shapes (white arrows in Fig. 2a). The periodicity of the pattern matches the period of the corrugations on the pillar surface, with a periodicity of 242 ± 5 nm. The SAED in Fig. 2c shows that the material is amorphous. The triangular pattern is approximately 80 nm in height and shows a sharp transition with the surrounding crystalline material. Amorphous material has already been observed close to ultra-short laser modifications of bulk sapphire [15, 16], as well as for longer pulses (300 ps) where the voids are also partially surrounded by polycrystalline phase [26]. In all three regimes, we did not record polycrystalline phase around the laser modification. In addition, the sharp transition between crystalline and amorphous phase induced by laser pulses has already been observed in previous studies in sapphire [15, 16], and the amorphous phase has been estimated as having the same or higher density than the crystalline phase [15, 17]. However, in our case, the amorphous phase has a lower density compared to the crystal sapphire, as indicated by a darker color in STEM-ADF images (see Suppl. Fig. S.2). This difference can be explained by the geometry of the process: while in references [15, 17], the modification is fully enclosed in the sapphire bulk, in our configuration, a significant fraction of the pressure is relaxed via material movement through the sample surface.

We also performed detailed investigations of the modifications below the surface. The bulk presents chaotic Bragg contrast lines close to the laser-modified region which indicate strain, as in within the white dashed oval of Fig. 2a. The strain is also observable in the SAEDs of the bulk which present small elongations in the diffraction spots, a sign of tiny rotations of the lattice compared to the main zone axis of the bulk, as well as in the KAM map (Suppl. Fig. S.3). Therefore, the energy deposited by the main lobe of the Bessel beam has an effect not only on the inner material rod but also on the surrounding sapphire.

To better understand the generation process, we analyzed the relative orientation of the crystalline lattice of the nano-pillar with the one of the bulk using TKD. The IPF figures provide the relative orientation between the different parts of the sample. In the case of the first regime, the IPF of the base of the pillar and part of the bulk is shown in Fig. 2d. The associated pole figure on the right shows, in combination with TKD data, that the pillar is only slightly rotated around its axis by approximately 4° compared to the bulk orientation (other pole figures in Suppl. Fig. S.3).

To conclude this section dedicated to the first regime, TEM imaging confirms that the first regime pillars are obtained through the *translation* of a solid rod of material. The mechanism is the following: the main lobe of the first-order Bessel beam generates a very thin, cylindrical layer of melted material. We estimate that the width of the melted cylindrical layer is on the order of a

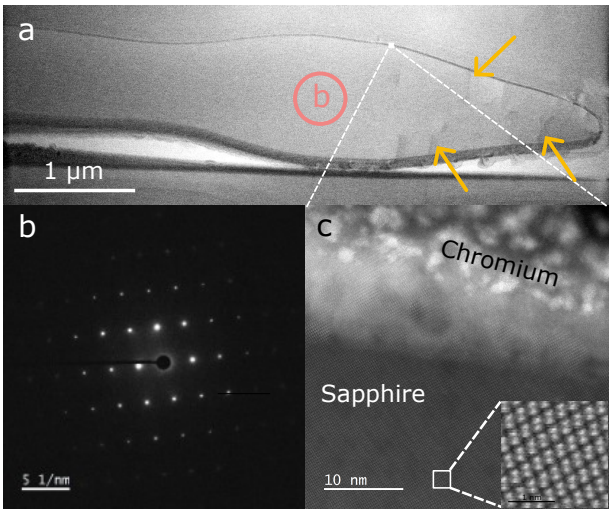

Fig. 3. (a) STEM-ABF images of the tip of the second regime nano-pillar. (b) SAED of the nano-pillar tip. (c) HR-STEM of the nano-pillar edge showing the crystalline sapphire and the protective chromium layer. The white dots in the inset show the disposition of the Al atoms.

few tens of nanometers. Within the pulse duration, the interference between the incoming and reflected part of the beam inscribes an additional periodic plasma pattern in the bulk and on the internal rod. Subsequently, heat diffusion and high pressure relax radially. This step produces defects visible in the TEM-BF images as chaotic Bragg contrast lines in the bulk close to the nano-pillar and on the nano-pillar edges. Afterwards, the higher pressure generated deeper in the bulk by the most intense part of the beam allows the extraction of the solid rod by a simple translation of material. Multiple observations support the hypothesis that the nano-pillar does not melt. Firstly, the nano-pillar is a monocrystal of sapphire, and its crystalline orientation is very close to the bulk one. The small mismatch is attributable to the rotation around the pillar axis during the translation. Secondly, while melting of the internal rod should have erased the previously formed pattern leaving a smooth surface, we observe the periodic pattern along the nano-pillar, indicating that no significant melting occurred in this regime.

4. Second regime: extrusion of viscous sapphire

The second regime is characterized by taller nano-pillars with a small wavy deformation at their tip. The nano-pillars in this regime present non-uniform diameters. In the case of this study (see Fig. 1e), the diameter varies from 0.66 µm at the bottom up to 1.2 µm at its top. The nano-pillar height is 12.7 µm, which exceeds the maximum height to be studied in a TEM foil. To overcome this problem, we studied the nano-pillar in two samples: after cutting the nano-pillar with the FIB, we prepared a first TEM foil to investigate the material properties of the upper part of the nano-pillar with the nano-pillar tip lying on the sapphire surface (Fig. 3), and a second to detail material modifications in the bulk below the nano-pillar (Fig. 4).

The pillar is homogeneous and crystalline until its tip as confirmed by the STEM-ABF image in Fig. 3a, and from the SAED in Fig. 3b (zone axis [-2 2 2]). The STEM-ABF image of Fig. 3a also shows some structural defects, as pointed out with yellow arrows. We also performed High Resolution STEM (HR-STEM) close to the edge of the nano-pillar. Fig. 3c shows the sharp edge of the crystalline structure which is adjacent to the protective layer of chromium. Importantly, no amorphous phase could be detected.

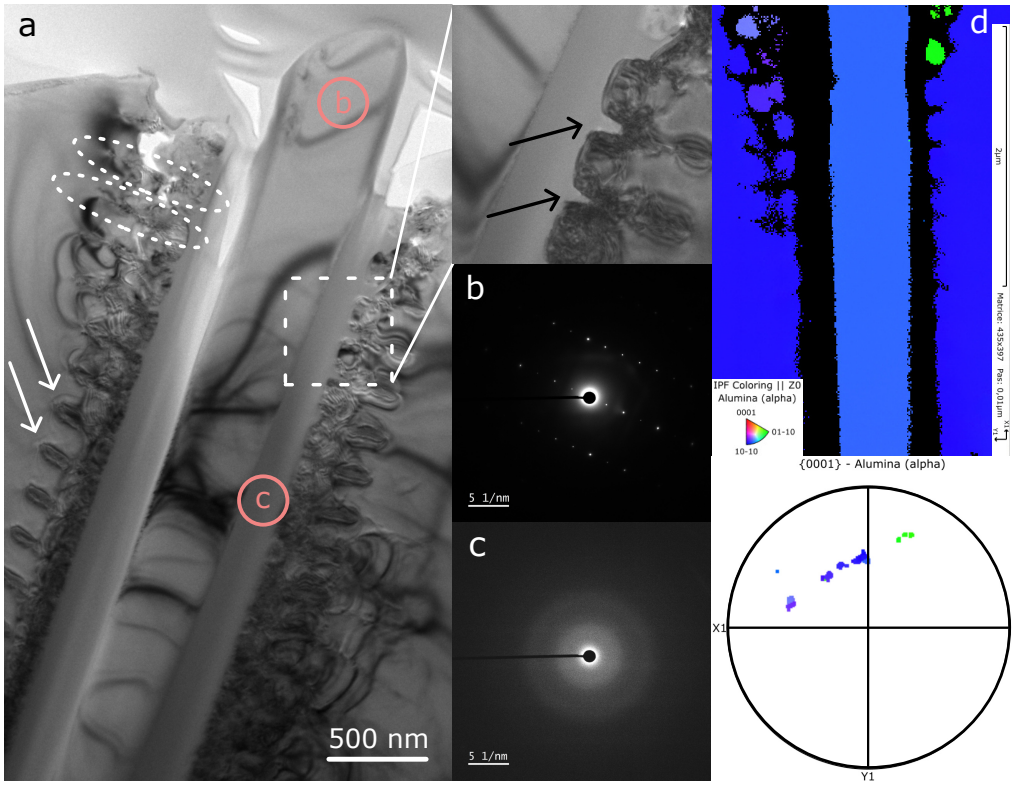

Fig. 4. TEM investigation of the bulk modification of the second regime nano-pillar. (a) TEM-BF image. (b-c) SAED of different parts of the modification. (d) IPF figure from TKD measurements of the pillar surrounded by the bulk and the relative pole figure.

The TEM-BF in Fig. 4a of the bulk modification shows a major difference which is the presence of two visible phases: the central rod with Bragg contrast lines, and a layer of surrounding material which does not show black lines. The SAEDs of the two regions confirm that the nano-pillar is crystalline sapphire also below the surface (Fig. 4b zone axis [9 3 0]) and the outer layer is completely amorphous (Fig. 4c). It is interesting to note that the diameter of the crystalline rod below the surface reduces by moving farther from the surface. Oppositely, the amorphous phase thickens (from 200 nm to 300 nm) but its external diameter remains constant at about 950 nm. In addition, the pillar is monocrystalline, homogeneous, and does not present defects (Suppl. Fig. S.5). The STEM-ADF investigations (Suppl. Fig. S.5) show that the transition from crystalline to amorphous phase is very sharp also in this regime. A faster cooling of the material in contact with the unaffected bulk sapphire explains the presence of the amorphous layer.

The IPF measurements in Fig. 4d compare the orientation of the crystalline structure of the nano-pillar to the bulk one (other pole figures are shown in Suppl. Fig. S.6). We observe small portions of the bulk with different orientations that probably moved during the pillar extraction. Moreover, the IPF indicates that the misorientation of the pillar compared to the bulk is larger than in the first regime. The TKD measurements suggest a rotation in the crystalline orientation of the pillar of about 12° around the pillar axis compared to the bulk.

As in the first regime, we observed strain close to the damaged zone as chaotic Bragg contrast lines and elongations in the diffraction spots in electron diffraction measurements (see Suppl. Fig. S.4). Compared to the previous regime, the elongations are more visible therefore the magnitude of the rotations of part of the crystalline lattice is higher, which is also confirmed by a greater

average misorientation (see KAM map in Suppl. Fig. S.6). In the second regime, the fluence on the rear surface is higher than in the previous regime. The energy deposition below the surface is accordingly higher, which creates more stress in the material.

As mentioned before, we can observe the periodic pattern in the bulk. The period of 243 ± 5 nm is compatible with the theoretical formula and with the values of the first regime. In this regime, we can distinguish two morphologies for the periodic pattern, which are better visible in the STEM images (Suppl. Fig. S.5). The first morphology has the triangle shape made of amorphous material as the one observed in the first regime (black arrows in close up of Fig. 4a). At the same depth of the first five triangles, the modifications are not limited to the amorphous part, but elongate farther from the center as a line of defects (Fig. 4a dashed oval, better visible in Suppl. Fig. S.5). Deeper in the bulk, we observe defects lines a bit farther from the modified area (white arrows in Fig. 4a, and in Suppl. Fig. S.5), where no amorphous phase was detectable. We infer that this lateral shift is due to the complex combination of ionization dynamics that reshapes the spatio-temporal shape of the laser pulse at sub-micrometric scales. The shift is approximately 250 nm, which is consistent with our previous investigations [25].

In the second regime, the fluence on the rear surface of the sample as well as close to the surface is higher compared to the first regime. Therefore, we expect that the internal rod reaches higher temperatures causing the mechanism of softening/melting. The material is ejected and it reaches a candle-like shape while cooling. The softening/melting and recrystallization of the rod are supported by the presence of a thick layer of amorphous material in the bulk and the absence of strain or defects at the nano-pillar edge. Rods of crystalline sapphire were already created from the melt with a very smooth surface when grown along the c-axis, as in our case [27].

As observed in the bulk, the softened/molten material has partially recrystallized and partially formed a vitrified state. The reason can be found in the cooling speed [28, 29]. The hollow cylinder directly affected by the laser beam has probably reached a higher temperature compared to the inner rod. This material is in contact with crystalline sapphire which has a high thermal conductivity ($k = 31\,\mathrm{W\,m^{-1}\,K^{-1}}$ which reduces by increasing the temperature [30]). Therefore, the rapid cooling of the material did not allow to form a crystalline pattern. In contrast, the internal rod is in contact with amorphous sapphire ($k = 2\,\mathrm{W\,m^{-1}\,K^{-1}}$ at ambient temperature [31]) or with air ($k = 0.02\,\mathrm{W\,m^{-1}\,K^{-1}}$ at ambient temperature [32]). Therefore, the internal rod is in contact with materials that have lower thermal conductivities, resulting in slower cooling and enabling recrystallization. The fact that the nano-pillar is a monocrystal suggests that the crystallization seed is unique. We suppose that the crystallization starts deep in the bulk (where the heat dissipates faster) and progresses toward the nano-pillar tip. The process reassembles the Bridgman method, where a seed of sapphire is used to grow a monocrystal from the melt by cooling the material through the solid sapphire [30]. For a nano-pillar of our dimension, an estimation of the speed of the crystallization front is around $440\,\mu\mathrm{m\,s^{-1}}$ [33]. This estimation falls in the conventional range of microcrystal growth speed [27, 34]. Despite being a monocrystal, the nano-pillar presents some defects at its tip. This recalls the Stepanov method in which liquid sapphire is pre-shaped and then cooled down to produce a monocrystal [30]. The resulting crystals can show blocks which are slightly misoriented compared to the growth axis, as well as some structural defects [30, 35]. Therefore, our observations support a mechanism based on sapphire softening, then reshaping, and subsequent resolidification.

5. Third regime: hydrodynamic jet of liquid sapphire

The nano-pillars belonging to the third regime are characterized by highly oscillating surfaces, which we linked to capillary instabilities [24]. The nano-pillar shown in Fig. 1f is representative of this regime: it has a nearly spherical shape with a diameter of 1.5 µm and an overall height of 5 µm, which makes the nano-pillar suitable to be studied in a single TEM foil.

The TEM-BF image of the nano-pillar is shown in Fig. 5a. The electron diffraction

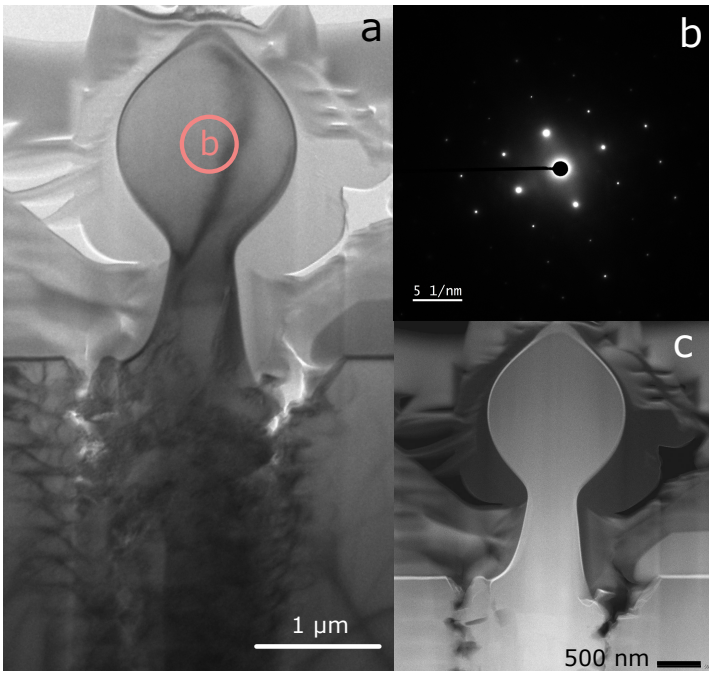

Fig. 5. (a) TEM-BF image of the nano-pillar of the third regime. (b) SAED of the central part of the nano-pillar. (c) STEM-ADF image of the nano-pillar.

measurement of the ball reveals that the nano-pillar is, also in this case, a monocrystal (SAED shown in Fig. 5b in the zone axis [11 4 1]). In addition, we performed STEM measurements: the STEM-ADF image of Fig. 5c shows a very homogeneous nano-pillar, and the STEM-ABF investigation does not show defects in the nano-pillar (Suppl. Fig. S.7). In the TEM-BF, the darker layer *i.e.* around the sphere is due to our deposition of chromium (confirmed with STEM-EDX (Energy-Dispersive X-ray) in Suppl. Fig. S.7).

Our measurements support a nano-pillar generation process of resolidification of a hydrodynamic jet of molten sapphire. Compared to the previous regime, the fluence of the main lobe at the rear surface is higher. Therefore, we expect the modified material to be at a higher temperature and, therefore, more fluid. The shapes of the nano-pillars match extremely well with hydrodynamic jets of molten sapphire and the related theoretical sizes [24]. The fact that the nano-pillar is a monocrystal suggests liquefaction and resolidification similar to that of the second regime. Therefore, the nano-pillar is shaped due to the capillary instabilities and then recrystallized from a single seed. The complete absence of defects in the third regime can be related to the longer cooling time of the pillar due to the high temperature of the melt and the pillar shape. In fact, a faster cooling of the melt is usually associated with the formation of defects [30].

6. Conclusions

TEM and TKD investigations allowed us to obtain structural information of the laser-generated nano-pillars on top of sapphire as well as of the regions modified in the bulk material below the nano-pillar. This structural information provides informative insights to confirm the scenario of nano-pillar formation for the three regimes. We could prove that, in the first regime, the nano-pillar is formed by a translation of material which remains mostly in the solid phase and slightly rotates around the nano-pillar axis. In contrast, in the second and third regimes, the

material forming the nano-pillar has been transiently melted before resolidification. It is striking that in both regimes, the final nano-pillar is also a monocrystal, even if its shape can be nearly spherical as for the case of the nano-pillar shown in Fig. 1f. This is explained by the slower cooling rate in air compared to bulk sapphire. Amorphous sapphire phase is observed only below the sample surface, in conditions where fast cooling is possible, *i.e.* in contact with un-excited sapphire or for highly localized nano-plasmas at 100 nm scale.

These results give a clearer picture of the nano-pillar formation mechanisms in laser-induced extrusion-like processes. Our results are of interest for applications that require specific properties of the pillar, as for understanding the complexity of the various processes that follow the laser-matter interaction.

Funding. This project has received funding from H2020 European Research Council (ERC) under grant agreement 682032-PULSAR, the European Union's Horizon 2020 research and innovation program under grant agreement No 825246 kW-flexiburst, the French Agence Nationale de la Recherche, projects DENSE (ANR-21-CE08-0005) and EQUIPEX+ SMARTLIGHT platform (ANR-21-ESRE-0040), and the EIPHI Graduate School (ANR-17-EURE-0002). This work was partially supported by the French Renatech network, MIMENTO technological facility, and the Région Bourgogne Franche-Comté.

Aknowledgments. Technical assistance by E. Dordor, M. Raschetti and R. Salut is gratefully acknowledged. AMSG and SSJ thank the consortium Lyon Saint Etienne de Microscopies and MANUTECH USD for the access to the TEM and FIB facilities respectively.

Disclosures. The authors declare no conflicts of interest.

Data availability. Data underlying the results presented in this paper are not publicly available at this time but may be obtained from the authors upon reasonable request.

Supplemental document. See Supplemental Material for supporting content.

References

1. J.-M. Shieh, Z.-H. Chen, B.-T. Dai, *et al.*, "Near-infrared femtosecond laser-induced crystallization of amorphous silicon," Appl. Phys. Lett. **85**, 1232–1234 (2004).
2. L. Rapp, B. Haberl, C. J. Pickard, *et al.*, "Experimental evidence of new tetragonal polymorphs of silicon formed through ultrafast laser-induced confined microexplosion," Nat. Commun. **6**, 7555 (2015).
3. I. M. Pinatti, A. F. Gouveia, C. Doñate-Buendía, *et al.*, "Femtosecond-laser-irradiation-induced structural organization and crystallinity of bi2wo6," Sci. Reports **10**, 4613 (2020).
4. K. Veenhuizen, S. McAnany, D. Nolan, *et al.*, "Fabrication of graded index single crystal in glass," Sci. Reports **7**, 44327 (2017).
5. J. Cao, L. Mazerolles, M. Lancry, *et al.*, "Modifications in lithium niobium silicate glass by femtosecond laser direct writing: morphology, crystallization, and nanostructure," J. Opt. Soc. Am. B **34**, 160–168 (2017).
6. J. S. Hoppius, D. Bialuschewski, S. Mathur, *et al.*, "Femtosecond laser crystallization of amorphous titanium oxide thin films," Appl. Phys. Lett. **113**, 071904 (2018).
7. A. Sharif, N. Farid, R. K. Vijayaraghavan, *et al.*, "Femtosecond laser assisted crystallization of gold thin films," Nanomaterials **11**, 1186 (2021).
8. M. Garcia-Lechuga, L. Haahr-Lillevang, J. Siegel, *et al.*, "Simultaneous time-space resolved reflectivity and interferometric measurements of dielectrics excited with femtosecond laser pulses," Phys. Rev. B **95**, 214114 (2017).
9. J. del Hoyo, R. Meyer, L. Furfaro, and F. Courvoisier, "Nanoscale confinement of energy deposition in glass by double ultrafast bessel pulses," Nanophotonics **10**, 1089–1097 (2020).
10. R. R. Gattass and E. Mazur, "Femtosecond laser micromachining in transparent materials," Nat. Photonics **2**, 219–225 (2008).
11. K. Falk, "Experimental methods for warm dense matter research," High Power Laser Sci. Eng. **6**, e59 (2018).
12. E. N. Glezer and E. Mazur, "Ultrafast-laser driven micro-explosions in transparent materials," Appl. Phys. Lett. **71**, 882–884 (1997).
13. S. Juodkazis, K. Nishimura, S. Tanaka, *et al.*, "Laser-induced microexplosion confined in the bulk of a sapphire crystal: Evidence of multimegabar pressures," Phys. Rev. Lett. **96**, 166101 (2006).
14. E. G. Gamaly, S. Juodkazis, K. Nishimura, *et al.*, "Laser-matter interaction in the bulk of a transparent solid: Confined microexplosion and void formation," Phys. Rev. B **73**, 214101 (2006).
15. S. Juodkazis, K. Nishimura, H. Misawa, *et al.*, "Control over the crystalline state of sapphire," Adv. Mater. **18**, 1361–1364 (2006).

16. V. Mizeikis, S. Kimura, N. V. Surovtsev, *et al.*, "Formation of amorphous sapphire by a femtosecond laser pulse induced micro-explosion," Appl. Surf. Sci. **255**, 9745–9749 (2009). Proceedings of the Sixth International Conference on Photo-Excited Processes and Applications (6-ICPEPA).
17. A. Vailionis, E. Gamaly, V. Mizeikis, *et al.*, "Evidence of superdense synthesized by ultrafast microexplosion," Nat. Commun. **2**, 445 (2011).
18. D. McGloin and K. Dholakia, "Bessel beams: Diffraction in a new light," Contemp. Phys. **46**, 15–28 (2005).
19. M. K. Bhuyan, F. Courvoisier, P. A. Lacourt, *et al.*, "High aspect ratio nanochannel machining using single shot femtosecond Bessel beams," Appl. Phys. Lett. **97**, 081102 (2010).
20. L. Rapp, R. Meyer, R. Giust, *et al.*, "High aspect ratio micro-explosions in the bulk of sapphire generated by femtosecond bessel beams," Sci. Reports **6**, 34286 (2016).
21. R. Meyer, L. Froehly, R. Giust, *et al.*, "Extremely high-aspect-ratio ultrafast bessel beam generation and stealth dicing of multi-millimeter thick glass," Appl. Phys. Lett. **114**, 201105 (2019).
22. H. D. Nguyen, A. Tsaturyan, S. S. Joao, *et al.*, "Quantitative Mapping of Transient Thermodynamic States in Ultrafast Laser Nanostructuring of Quartz," Ultrafast Sci. **4**, 0056 (2024).
23. C. Xie, V. Jukna, C. Milian, *et al.*, "Tubular filamentation for laser material processing," Sci. Reports **5**, 8914 (2015).
24. V. V. Belloni, M. Hassan, L. Furfaro, *et al.*, "Single shot generation of high-aspect-ratio nano-rods from sapphire by ultrafast first order Bessel beam," Laser & Photonics Rev. **18**, 2300687 (2023).
25. K. Ardaneh, R. Meyer, M. Hassan, *et al.*, "High energy density plasma mediated by collisionless resonance absorption inside dielectrics," arXiv preprint 2109.00803v2 (2022).
26. V. Nguyen, Z. Rehman, K. Janulewicz, and H. Suk, "Dynamics of laser-induced phase transformation in bulk of monocrystalline sapphire," Results Phys. **40**, 105848 (2022).
27. H. E. Labelle and A. I. Mlavsky, "Growth of sapphire filaments from the melt," Nature **216**, 574–575 (1967).
28. D. Turnbull, "Under what conditions can a glass be formed?" Contemp. Phys. **10**, 473–488 (1969).
29. P. G. Debenedetti and F. H. Stillinger, "Supercooled liquids and the glass transition," Nature **410**, 259–267 (2001).
30. E. R. Dobrovinskaya, L. A. Lytvynov, and V. Pishchik, *Sapphire*, Micro- and Opto-Electronic Materials, Structures, and Systems (MOEM) (Springer, 2009).
31. A. Abdullaev, V. S. Chauhan, B. Muminov, *et al.*, "Thermal transport across nanoscale damage profile in sapphire irradiated by swift heavy ions," J. Appl. Phys. **127**, 035108 (2020).
32. Y. S. Touloukian, R. W. Powell, C. Y. Ho, and P. G. Klemens, "Thermophysical properties of matter - the TPRC data series. volume 2. thermal conductivity - nonmetallic solids," (1971).
33. G. Lebedev, S. Malyukov, V. Stefanovich, and D. Cherednichenko, "Thermophysical processes during sapphire crystal growth by the horizontal Bridgman method," Crystallogr. Reports **53**, 331–335 (2008).
34. J. Malek, J. Shanelova, S. Martinkova, *et al.*, "Crystal growth velocity in As2Se3 supercooled liquid," Cryst. Growth & Des. **17**, 4990–4999 (2017).
35. V. Krymov, Y. G. Nosov, S. Bakholdin, *et al.*, "Blocks and residual stresses in shaped sapphire single crystals," J. Cryst. Growth **457**, 314–319 (2017).